ACES Asian Chemical Editorial Society

doi.org/10.1002/cnma.202100281

CHEMNANOMAT
Full Paper

Local Structure of Europium-Doped Luminescent Strontium Fluoride Nanoparticles: Comparative X-ray Absorption Spectroscopy and Diffraction Study

Kirill V. Yusenko,*[a] Anke Kabelitz,[a] Alexander Schökel,[b] Ralph Wagner,[c] Carsten Prinz,[a] Erhard Kemnitz,[d] Franziska Emmerling,[a] Thoralf Krahl,[e] and Ana Guilherme Buzanich*[a]

Abstract: Rare-earth based luminescent materials are key functional components for the rational design of light-conversion smart devices. Stable Eu^{3+}-doped strontium fluoride (SrF_2) nanoparticles were prepared at room temperature in ethylene glycol. Their luminescence depends on the Eu content and changes after heat treatment. The crystallinity of heat-treated material increases in comparison with as-synthesized samples. Particles were investigated in solution using X-ray diffraction, small-angle X-ray scattering, and X-ray spectroscopy. After heat treatment, the size of the disordered nanoparticles increases together with a change of their local structure. Interstitial fluoride ions can be localized near Eu^{3+} ions. Therefore, non-radiative relaxation from other mechanisms is decreased. Knowledge about the cation distribution is key information for understanding the luminescence properties of any material.

Introduction

The mineral fluorite CaF_2 is the most abundant fluorine containing mineral. It is eponymous for the cubic fluorite structure type. Apart from CaF_2, other metal fluorides SrF_2, BaF_2, CdF_2 and β-PbF_2 crystallize in the same structure type (and probably also RaF_2). Naturally occurring *fluorite* rarely occurs as pure colorless CaF_2, but incorporates several other metal ions and defects, resulting in various colored mineral types.[1]

Fluorite type metal fluorides MF_2 (M = Ca, Sr, Ba, Cd, Pb) can incorporate significant amounts of trivalent rare-earth metal fluorides LnF_3 (Ln = Y, La–Lu).[2] Solid solutions of LnF_3 in MF_2 are formed up to an amount of ≈45% Ln-content, adopting a stoichiometry $M_{1-x}Ln_xF_{2+x}$ (x = 0–≈0.45) and retaining the cubic fluorite structure. The equilibrium phase diagram SrF_2–EuF_3 is presented as a typical example in Figure 1.[3,4]

These solid solutions are of interest for material science. Compared to pure MF_2 materials, they exhibit increased microhardness and greatly increased ionic conductivity.[5,6] The latter feature allows their application in batteries.[7] Furthermore, especially CaF_2 and SrF_2 are excellent host materials for trivalent luminescent rare-earth metal ions.[8–12]

The structure of these materials has been investigated for long time. CaF_2 itself can be regarded as a cubic-closest packing of calcium ions, where the tetrahedral gaps are occupied by fluoride ions (cubic space group $Fm\bar{3}m$ (225)). Solid solutions $Ca_{1-x}Ln_xF_{2+x}$ with fluorite structure possess surplus fluoride ions for charge compensation. They occupy different positions in the

[a] Dr. K. V. Yusenko, Dr. A. Kabelitz, C. Prinz, PD Dr. F. Emmerling, Dr. A. Guilherme Buzanich
BAM Federal Institute for Materials Research and Testing
Richard-Willstätter Str. 11, 12489 Berlin (Germany)
E-mail: kirill.yusenko@bam.de
ana.buzanich@bam.de

[b] Dr. A. Schökel
Deutsches Elektronen-Synchrotron (DESY)
Notkestr. 85, 22607 Hamburg (Germany)

[c] R. Wagner
Materialwissenschaften Fachgruppe Physik Fachbereich C
Bergische Universität Wuppertal
Gaußstraße 20, 42097 Wuppertal (Germany)

[d] Prof. Dr. E. Kemnitz
Institut für Chemie
Humboldt-Universität zu Berlin
Rudower Chaussee 29, 12489 Berlin (Germany)

[e] Dr. T. Krahl
Nanofluor GmbH
Rudower Chaussee 29, 12489 Berlin (Germany)

Supporting information for this article is available on the WWW under https://doi.org/10.1002/cnma.202100281

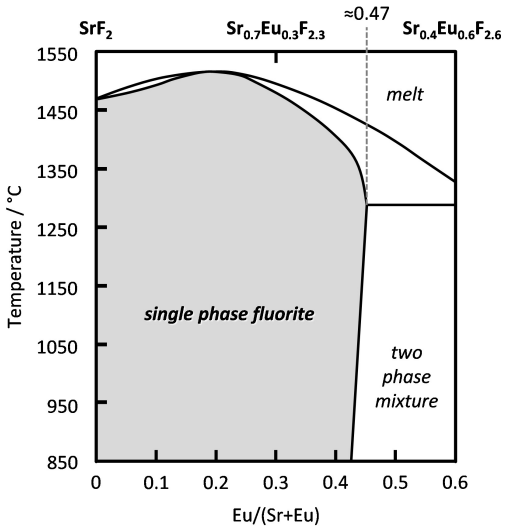

Figure 1. Sr-rich part of the equilibrium phase diagram SrF_2-EuF_3. Phase diagrams of all combinations MF_2-LnF_3 (M = Ca, Sr; Ln = Y, La–Lu) are qualitatively similar.[3]

octahedral gap, which are unoccupied in perfect CaF_2. At rare-earth ion contents above 1 at.%, *i.e.* $x \geq 0.01$, the surplus fluoride ions form clusters around unoccupied regular tetrahedral fluoride positions.[13–15] The nature of the clusters depends on the size of rare-earth metal ion (Figure 2). For lager ions La^{3+}–Nd^{3+}, surplus fluoride ions are located on the crystallographic 32*f* position forming triangular clusters. For smaller ions Dy^{3+}–Lu^{3+} and Y^{3+}, surplus ions are located on the crystallographic 48*i* position forming cubeoctahedral clusters. Some authors find an additional 13th fluoride ion inside this cluster, while others do not.[16,17] For the intermediate sized ions, both types may occur. Less work was done on SrF_2, but the effects are mainly the same.[18,19]

While the nature of the clustering of fluoride ions is thoroughly investigated, little is known about the cation distribution. It is common sense that the alkaline earth metal ions and the rare-earth metal ions share regular cation lattice sites. ^{89}Y solid state NMR on annealed $Ca_{1-x}Y_xF_{2+x}$ hints that concentration of Y^{3+} near fluoride clusters is higher than expected for a purely statistical distribution, especially for high Y-contents of 20 at.% and above.[20] Luminescence of $Ca_{1-x}Eu_xF_{2+x}$ precipitated from aqueous solution also hints to a non-statistical distribution due to strong luminescence quenching for Eu-contents above 15 at.%.[21,22] Additionally, the cation distribution depends on the synthesis method.[8,9]

Understanding about the cation distribution is an important point rationalizing the properties of such materials. In this study, a series of transparent dispersions (sols) of $Sr_{1-x}Eu_xF_{2+x}$ nanoparticles in ethylene glycol (b.p. 195 °C) with $x = 0$, 0.01, 0.02, 0.05, 0.1, 0.2, 0.3, 0.4 was-synthesized by fluorolytic sol gel synthesis at room temperature. A fraction of each sol was annealed at 160 °C for two hours. Both series of samples were investigated by X-ray absorption spectroscopy (XANES/EXAFS) of the Sr–K and Eu–L_3 absorption edges, synchrotron X-ray diffraction (XRD), small angle X-ray scattering (SAXS) and photoluminescence emission (PLE). Comparison of the results for both sample series allows insights into the cation distribution at different temperatures.

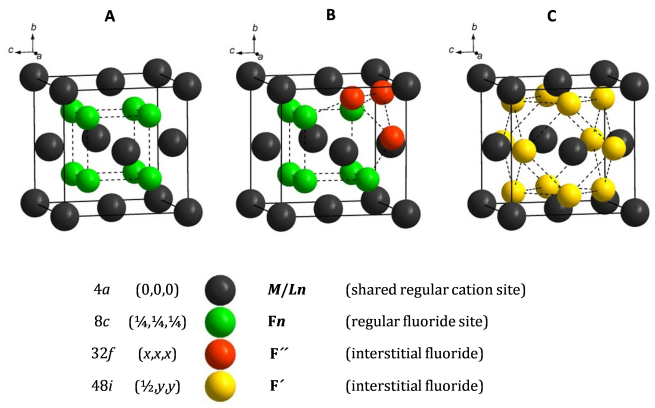

Figure 2. Fluoride clusters found in solid solutions MF_2-LnF_3 ($M_{1-x}Ln_xF_{2+x}$; $x = 0$–≈ 0.45; M = Ca, Sr; Ln = Y, La–Lu). Wyckoff symbols are for space group $Fm\bar{3}m$ (225). (**A**) Undisturbed fluorite structure of MF_2 ($x = 0$). (**B**) Triangular cluster defects for 32*f* positions ($x \geq 0.01$). (**C**) Cubeoctahedral cluster defects for 48*i* positions ($x \geq 0.01$).[13–15]

Results and Discussion

Luminescent properties of $Sr_{1-x}Eu_xF_{2-x}$ ($x = 0$, 0.01, 0.02, 0.05, 0.1, 0.2, 0.3, 0.4) nanoparticles show significant changes with Eu^{3+} content as well as temperature annealing. To support luminescent measurements and understand changes in local structure and morphology, X-ray diffraction, X-ray small-angle scattering, and X-ray spectroscopy studies were performed.

Synthesis

The synthesis of $Sr_{1-x}Eu_xF_{2+x}$ nanoparticles is straightforward and leads to transparent sols in ethylene glycol. Transparency of the sol's hints to deagglomerated particles with a size below 25 nm. A thorough discussion of the synthesis can be found elsewhere.[11] The overall cation concentration in the final sol is 300 mM. Thus, europium concentration increases from 3 mM for $Sr_{0.99}Eu_{0.01}F_{2.01}$ to 120 mM for $Sr_{0.60}Eu_{0.40}F_{2.40}$.

The sols contain small amounts of water (≈1%), methanol (≈2%), lactic acid and acetic acid (both together ≈5%) and were used without further purification. Small amounts of water may be additionally formed due to esterification. Annealing of the sols is performed at 160 °C, which is below the boiling point of ethylene glycol (195 °C). The pressure inside the Teflon vessel raises maximum to 1.5 atmospheres. The solubility of the metal fluorides in ethylene glycol is far below the solubility in water (SrF_2: 160 mg/L, EuF_3: < 10 mg/L in H_2O). Due to the small amounts of water and low pressure, solvothermal reactions can be ruled out. Dispersions are still transparent and colorless after annealing. Eu(II) species cannot be obtained after synthesis due to absence of strongly reducing agents. Luminescence spectra can be fully explained by emission of Eu^{3+}.

Luminescent properties

Figure 3 presents the PL emission spectra of both series of samples. Excitation spectra are found in the SI Figure S1. The emission spectra exhibit narrow lines due to radiative $^5D_0 \rightarrow {}^7F_J$ transitions of the Eu^{3+} ion (Figure 4a). The transitions $J = 1$, 2, 4 with maxima at 590, 615, and 698 nm, respectively, are allowed and comparatively intensive. The forbidden transition $J = 0$ is expressed at a shoulder centered at 580 nm, the forbidden transition $J = 3$ is weakly expressed with a maximum at 648 nm. No emission of Eu^{2+} is observed (expected broad intensive emission line between 400 and 450 nm).[23] Spectra for both series are qualitatively similar. However, differences occur in luminescence intensity (Figure 5).

For the as-synthesized series, there is linear increase of the luminescence intensity up to 10 at.% Eu^{3+}. Above 10 at.% contents, luminescence intensity still increases but deviates from linearity. This is the typical behavior observed for samples

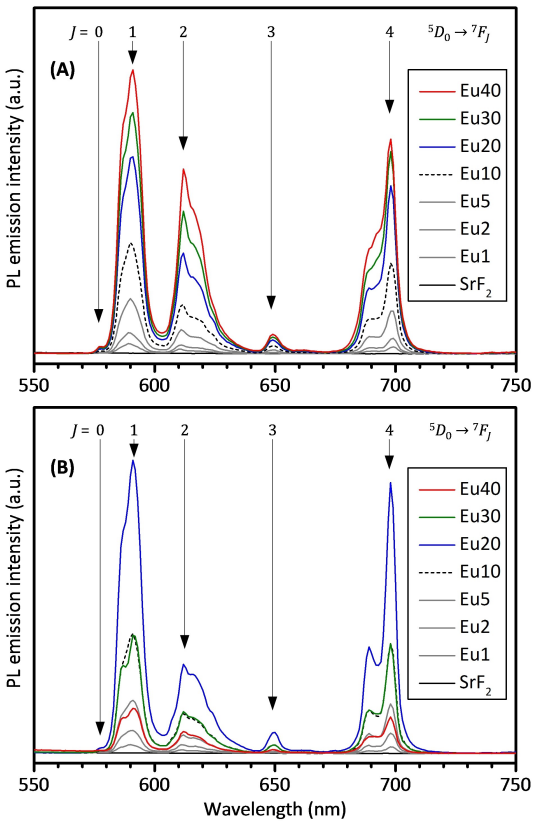

Figure 3. PL emission spectra of 0.3 M sols of $Sr_{1-x}Eu_xF_{2+x}$ in ethylene glycol (λ_{ex} = 393 nm). (A) as-synthesized, (B) annealed at 160 °C.

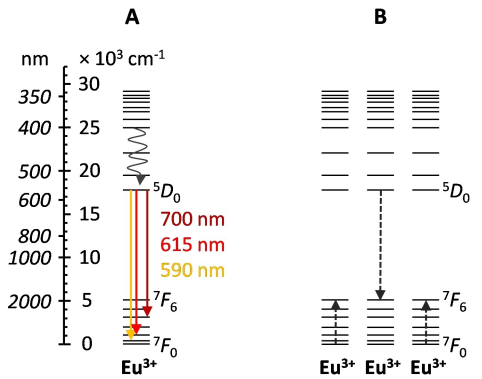

Figure 4. (A) Simplified energy level diagram of Eu^{3+} emission showing $^5D_0 \rightarrow {}^7F_J$ transitions. Forbidden transitions J = 0, 3 are omitted for clarity. (B) Simplified energy level diagram illustrating non-radiative cross-relaxation between three neighboring Eu^{3+} ions. Note that relaxation between two Eu^{3+} ions only is not possible due the lack of an appropriate energy level.

from the fluorolytic sol-gel synthesis.[11,24] Increasing emission intensity is due to increasing total content of Eu^{3+} in the sol. Deviation from linearity is caused by a tiny amount of non-radiative cross-relaxation (Figure 4 and below).

For the series annealed at 160 °C, luminescence intensity also increases nearly linearly up to 20 at.% Eu^{3+}. Additionally, the luminescence intensity is higher than for the as-synthesized samples. Prominently, $Sr_{0.80}Eu_{0.20}F_{2.20}$ shows the highest emission

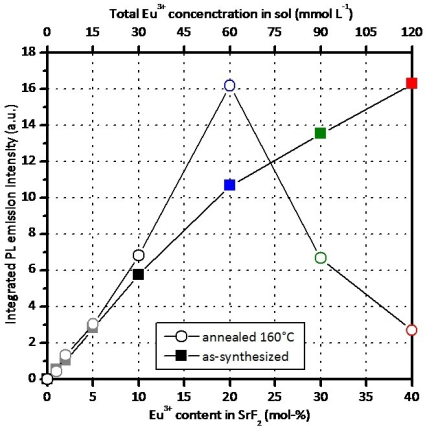

Figure 5. Integrated PL emission intensity (570–720 nm) of 0.3 M sols of $Sr_{1-x}Eu_xF_{2+x}$ in ethylene glycol (λ_{ex} = 393 nm).

intensity more than 2.5 times that of $Sr_{0.90}Eu_{0.10}F_{2.10}$. The reasons for this outstanding behavior are not fully understood. However, the higher intensity of the annealed samples compared to the as-synthesized ones can be explained by a higher degree of "crystallinity". During the thermal annealing, lattice defects others than fluoride clusters (Figure 2) and surface defects are healed, and hence, leading to lower rate of non-radiative radiation into lattice vibrations. Additionally, particle growth during annealing may lead to a lower non-radiative relaxation rate through the surface due to a lower surface-to-volume ratio. Surprisingly, the emission intensity of $Sr_{0.70}Eu_{0.30}F_{2.30}$ and $Sr_{0.60}Eu_{0.40}F_{2.40}$ drops drastically upon thermal treatment, with $Sr_{0.60}Eu_{0.40}F_{2.40}$ being even less intensive than $Sr_{0.70}Eu_{0.30}F_{2.30}$. In general, this trend is also observed for samples precipitated from aqueous solutions.[21,22]

These trends of luminescence intensity are in good agreement with the measured lifetimes of the excited Eu^{3+} state $^5D_0$, from which luminescence occurs. For all samples (annealed and as-synthesized) with Eu^{3+} contents from 1 at.% to 10 at.%, the lifetime is roughly ≈3.5 ms (Table 1). Samples with an intensity below the linear trend (20 at.%–40 at.% as-synthesized) show lifetimes below 3 ms. For the annealed sample $Sr_{0.80}Eu_{0.20}F_{2.20}$, its high luminescence intensity correlates with a lifetime above 4 ms.

Table 1. . Mean luminescence lifetimes $\bar{\tau}$ (biexponential decay) of the $^5D_0$ level of Eu^{3+} in 0.3 M $Sr_{1-x}Eu_xF_{2+x}$ in ethylene glycol. For comparison: lifetime of 20 mM solution of $Eu(OAc)_3$ in ethylene glycol is 0.345 ms (monoexponential decay).

Eu (at.%)	as-synthesized	annealed 160 °C
1	3.93 ms	3.66 ms
2	3.81 ms	3.49 ms
5	3.50 ms	3.68 ms
10	3.31 ms	3.89 ms
20	2.74 ms	4.17 ms
30	2.29 ms	1.36 ms
40	2.24 ms	0.39 ms

The dramatic decrease of the luminesce intensity for annealed samples with 30 at.% or 40 at.% Eu^{3+} is accompanied by very short lifetimes of ≈1.4 and ≈0.4 ms, respectively. The only relaxation mechanism leading to these short lifetimes is cross-relaxation between three neighboring Eu^{3+} ions (Figure 4B).[25] Schematically, the quenching effect can be formulated as follows:

$$Eu^{3+}(^5D_0) + 2\,Eu^{3+}(^7F_0) \rightarrow 3\,Eu^{3+}(^7F_J), \text{ with } J = 4 - 6.$$

Relaxation between two neighboring Eu^{3+} is not possible in this way due to the lack of appropriate energy levels. Thus, this type of cross-relaxation only occurs for comparatively high Eu^{3+} contents and for non-uniform distributions of Eu^{3+} through the lattice. Hence it can be concluded that the distribution of Eu^{3+} through the cation sites is nearly statistical for the as-synthesized samples. For the annealed samples, cation diffusion occurs. The distribution of Eu^{3+} through the cation sites is not statistical anymore, but Eu^{3+} ions start to cluster themselves. From a thermodynamic point of view, these Eu^{3+} rich regions are expected spatially near the fluoride clusters (Figure 2) due to a lower Coulomb energy.

X-ray diffraction study

The $Sr_{1-x}Eu_xF_{2+x}$ particles have relatively low concentration and are distributed in media with relatively high scattering power. As a result, in house X-ray diffraction study provides insufficient information about structure and size of the material. Nevertheless, high-energy X-ray diffraction allows to obtain experimental data suitable for Rietveld refinement as well as subtract background and obtain information about high-order diffraction lines. All samples show similar diffractograms which after background subtraction correspond to the pure fluoritic SrF_2 (Figure S2). No additional diffraction peaks corresponding to tysonite EuF_3 hexagonal structure were observed. After heat-treatment, narrower diffraction lines indicating higher crystallinity were observed. Interstitial fluorides which might correspond to additional positions should be disordered between 4 or 6 positions with lower occupancy with relatively large asymmetric thermal factors (Figure 2). The diffraction data cannot unambiguously differentiate between additional interstitial positions. In all discussed samples, the best fits were obtained for interstitial fluorine located in $F_i = {}^1/_2\ {}^1/_2\ {}^1/_2$. The following model has been applied for data refinement (after background subtraction):

$$Sr = 0\ 0\ 0 \mid occSr = 1 - occEu$$

$$Eu = \ 0\ 0\ 0 \mid occEu = occEu$$

$$F_1 = {}^1/_4\ {}^1/_4\ {}^1/_4 \mid occF_1 = 1$$

$$F_i = {}^1/_2\ {}^1/_2\ {}^1/_2 \mid occF_i = occEu$$

The cell parameter *a* (Table 2) systematically decreases with Eu concentration which is in accordance with data obtained for $Sr_{1-x}Eu_xF_{2+x}$ bulk phases prepared for SrF_2–EuF_3 binary phase diagram evaluation in its solidus part. Cell parameters for annealed samples are slightly smaller in comparison with as-synthetized particles. Averaged particles size is growing as well as crystallographic strain is decreasing with annealing which indicates an annealing of all defects during heating (Figure 6).

Trends in crystallite size (size of the coherent scattering region estimated by the diffraction line broadness) as well as in crystallographic strain are strictly depend on Eu content and change after annealing. Before annealing, the crystallite size with low Eu composition (below 30 at.% Eu) is close to 10 Å; above 30 at.% Eu, particles are a bit large. After annealing, the crystallite size is drastically increased for low Eu composition with decreasing number from $Sr_{0.99}Eu_{0.01}F_{2.01}$ to $Sr_{0.8}Eu_{0.2}F_{2.2}$. For $Sr_{0.7}Eu_{0.3}F_{2.3}$ and $Sr_{0.6}Eu_{0.4}F_{2.4}$, particle size is growing from 1.7 to 2.2 nm but does not depend on Eu concentration. Crystallographic strain grows with Eu concentration due to differences in ionic radii characteristic for Sr^{2+} and Eu^{3+} and presence of interstitial fluorine anions.

Particle size and particle size distribution from SAXS data and TEM

All measured small-angle X-ray scattering data are summarized in Figure S3. All SAXS data can be fitted using a model function that describes a particle as homogeneous sphere with its average radius (*Ra*) with a Schulz-Zimm distribution of particles

Table 2. Cell parameters (*a*) for cubic $Sr_{1-x}Eu_xF_{2+x}$ particles; Lorentzian crystallites size, and Lorentzian strain obtained from Rietveld refinement; particle diameter ($D = 2Ra$) and particle size distribution (sig) for as synthetized and annealed $Sr_{1-x}Eu_xF_{2+x}$ particles obtained from small-angle X-ray scattering data fits.

Composition	Rietveld refinement as synthetized			annealed			Small-angle X-ray scattering as synthetized		annealed	
	a, Å	size, nm	strain	*a*, Å	size, nm	strain	$D = 2Ra$, nm	*sig*, nm	$D = 2Ra$, nm	*sig*, nm
$Sr_{0.6}Eu_{0.4}F_{2.4}$	5.836(2)	1.6(2)	1.2(2)	5.831(2)	2.3(4)	1.0(1)	2.5(1)	0.28(5)	3.7(1)	0.26(5)
$Sr_{0.7}Eu_{0.3}F_{2.3}$	5.847(1)	1.8(1)	0.9(1)	5.838(1)	2.2(3)	1.0(1)	2.5(1)	0.29(5)	3.5(1)	0.29(5)
$Sr_{0.8}Eu_{0.2}F_{2.2}$	5.856(1)	1.02(8)	1.11(15)	5.847(1)	1.8(1)	0.9(1)	2.5(1)	0.25(5)	3.5(1)	0.25(5)
$Sr_{0.9}Eu_{0.1}F_{2.1}$	5.864(1)	1.05(5)	0.98(8)	5.8579(9)	1.77(10)	0.52(6)	2.0(1)	0.31(5)	3.5(1)	0.25(5)
$Sr_{0.95}Eu_{0.05}F_{2.05}$	5.8671(7)	1.00(3)	0.48(7)	5.8593(7)	2.40(14)	0.43(5)	2.4(1)	0.30(5)	3.4(1)	0.42(5)
$Sr_{0.98}Eu_{0.02}F_{2.02}$	5.8691(9)	1.08(4)	0.36(6)	5.8629(6)	2.63(15)	0.39(4)	2.2(1)	0.35(5)	3.5(1)	0.55(5)
$Sr_{0.99}Eu_{0.01}F_{2.01}$	5.8690(8)	0.96(3)	0.14(7)	5.863(1)	3.37(70)	0.56(12)	2.2(1)	0.38(5)	3.4(1)	0.55(5)
pristine SrF_2	–	–	–	–	–	–	2.1(1)	0.39(5)	3.3(1)	0.66(5)

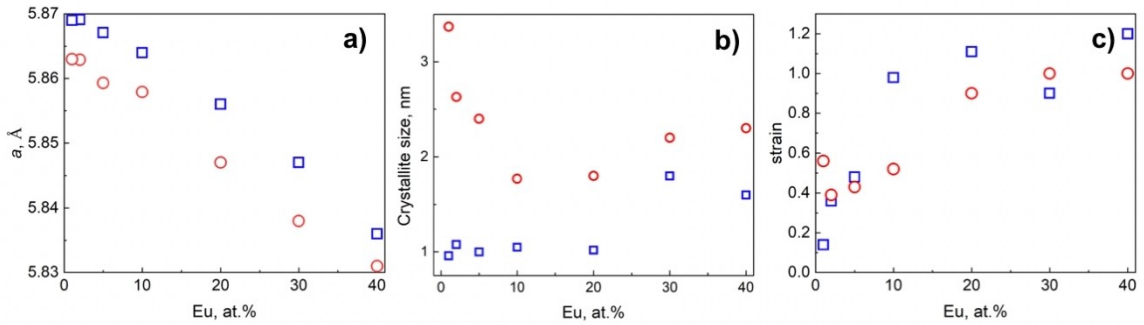

Figure 6. Rietveld refinement data (cell parameters (a), particle size (b) and crystallographic strain (c) for as-synthesized (□) and annealed (o)) for $Sr_{1-x}Eu_xF_{2+x}$ samples (according to Table 2).

radii (*sig*) (Table 2). For all compositions, sol particles seem to be too large with relatively broad size and shape distribution to show scattering curves at higher Q range above 200 nm^{-1}. For as synthetized and annealed samples, particle size does not depend on Eu concentration. Particle radii are growing after annealing from 2.2–2.3 nm for as synthetized particles; for annealed samples, average particle radii can be estimated as about 3.5 nm (Figure 7). Particle size distribution for samples with small Eu content (below 10 at.% Eu) is decreasing with growing Eu composition and increases after annealing. For samples with larger Eu content (above 10 at.% Eu), particle size distribution does not change with Eu content and does not change after annealing.

Average particles size, particles size distribution and crystallographic stress obtained from wide- and small-angle X-ray scattering data support findings obtained using luminescence data. As synthetized samples show relatively large size according to small angle scattering but smaller size according to wide-angle scattering. The difference might be explained by existence of structural defects such as twins and planar defects as well as influence of Eu^{3+} distribution on diffraction lines broadening. Similar results obtained by both techniques after annealing show more ideal sol particles with relatively narrow size distribution. Sol particles with large Eu content (above 10 at.% Eu) are stable and do not change their particle size distribution with either composition nor annealing.

Similar trend can be directly observed from transmission electron microscopy images (Figure 8). TEM images show crystalline particles nicely dispersed in the solution. Isolated nanoparticles have size below 2–3 nm for as synthetized samples. After heat treatment, particles size increase. Particle sizes derived from SAXS are larger than the crystallite sizes determined from XRD. Thus, the particle consists of a small crystalline core embedded in to a more or less amorphous shell.

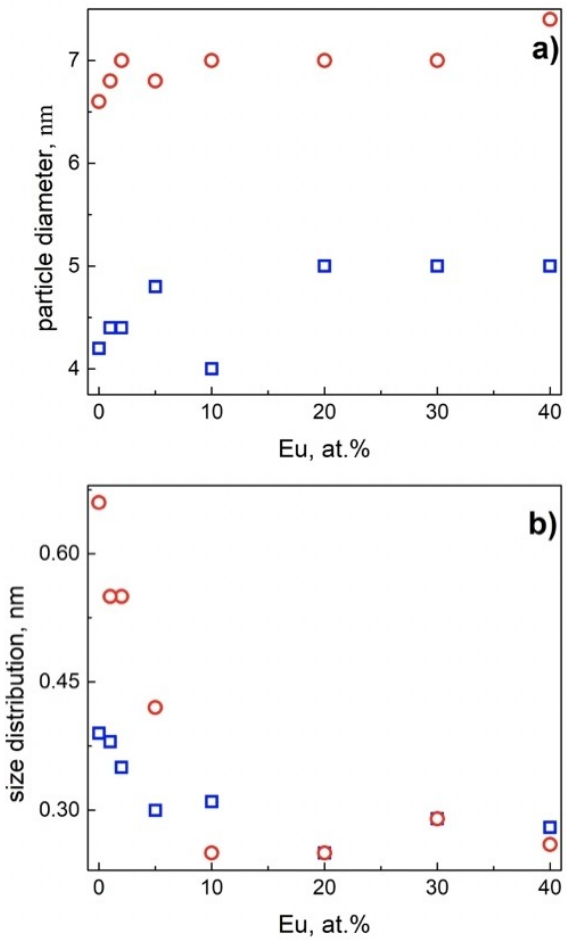

Figure 7. Average particle diameter ($D = 2Ra$, a) and particle size distribution (*sig*, b) for as synthetized (□) and annealed (o) $Sr_{1-x}Eu_xF_{2+x}$ samples obtained using small-angle X-ray scattering (according to Table 2).

Local environment from XAS data

All samples were characterized using XAS data obtained for Sr–K (16.105 keV) and Eu–L_3 (6.977 keV) edges (Figure 9). In Sr–K EXAFS spectra, the coordination environment below 5.1 Å includes Sr–F_8 cube of the first coordination sphere occupied by normal fluoride ($F_1 = {}^1/_4\ {}^1/_4\ {}^1/_4$; Sr–F = 2.51 Å), Sr–$F_6$ octahedron of the first coordination sphere occupied by interstitial fluoride ($F_i = {}^1/_2\ {}^1/_2\ {}^1/_2$; Sr–F = 2.90 Å), Sr…$Sr_{12}$ cuboctahedron occupied by Sr or Eu with Sr…Sr = 4.10 Å, Sr…F_{24} of the second

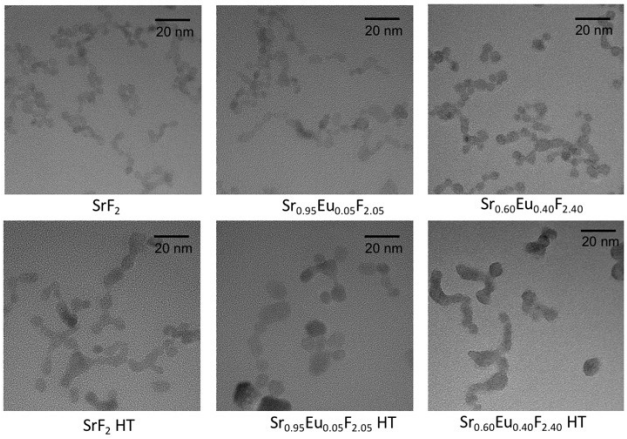

Figure 8. Selected TEM images of $Sr_{1-x}Eu_xF_{2+x}$ nanoparticles

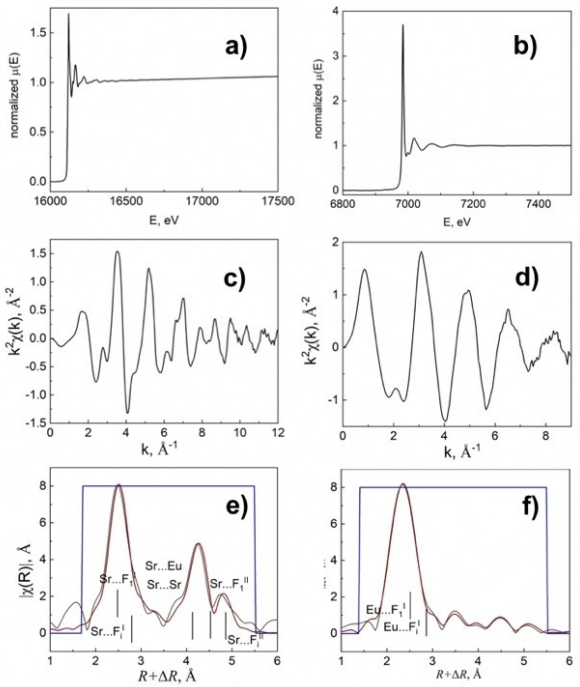

Figure 9. EXAFS spectra for as-synthetized $Sr_{0.8}Eu_{0.2}F_{2.2}$ sample in energy range (a and b), *k*-range (c and d).Left (a, c, e): Sr–K (16.105 keV) edge; right (b, d, f): Eu–L_3 (6.977 keV) edge. In Sr–K edge spectra, first F^I and second F^{II} coordination spheres should be considered. Fourier transformed experimental (black) and fitted (red) curves (e and f) correspond R-windows of 1.7–5.5 Å (Sr–K edge,) and 1.4–5.5 Å (Eu-L_3 edge) (blue lines). For Sr–K edge spectrum (e): R = 0.20%, reduced χ^2 = 435.8, number of independent points = 23, number of variables = 12; for Eu-L_3 edge spectrum (f): R = 0.24%, reduced χ^2 = = 56.8, number of independent points = 18, number of variables = 12.

coordination sphere occupied by F_1 fluoride with Sr…F = 4.81 Å and Sr…F_8 cube of the second coordination sphere occupied by interstitial fluoride F_i with Sr…F = 5.02 Å (Figure 2). Sr–K EXAFS spectra were fitted in the *R* range 1.7–5.5 Å. In Eu–L_3 EXAFS spectra, there is only the first coordination sphere occupied by F_1 and interstitial F_i anions can be detected below R_{max} = 3.0 Å (EuF_8 cube and EuF_6 octahedron). The Sr–K EXAFS spectrum of pristine Eu-free SrF_2 nanoparticles can be fitted using the ideal fluorite structure with only F_1 fluoride anions (Figure 10). Consequently, two Sr…F and one Sr…Sr single scattering paths and forward double scattering paths should be considered. For Eu-containing $Sr_{1-x}Eu_xF_{2+x}$ nanoparticles, additional two Sr…F scattering paths corresponding to interstitial fluoride in F_i position as well as 4 forward and double scattering paths should be considered. Cell parameters were taken from powder X-ray diffraction refinements (see Table 2). For spectra modelling, *sigma*^{2} has been refined for each scattering path individually as well as number of interstitial fluoride anions in F_i position and Eu in Sr position in the coordination environment of Sr were refined independently. In total, 12 variables were refined for Sr–K EXAFS spectra, starting value for the amplitude has been obtained from the fit of pristine SrF_2 sample. Refined parameters for all samples are summarized in Tables S1 and S2.

Eu–L_3 EXAFS spectra were fitted using F_1 and F_i fluoride anions located in the same crystallographic positions as for Sr–K refinement. N_{F1} and N_{Fi} were also fitted for all Eu–L_3 XAFS spectra in the *R*-range 1.4–5.5 Å (Tables S1 and S2).

The local environment characteristic for Sr atoms in the crystal structure can be estimated based on refinements based on Sr–K EXAFS spectra. In the ideal case, with increasing number of Eu atoms around Sr their coordination number should linearly increase from N_{Eu} = 0 (other positions should be occupied by 12 Sr) for pristine SrF_2 to $N_{Eu} = 0.4 \times 12 = 2.4$ for $Sr_{0.6}Eu_{0.4}F_{2.4}$ (maximum coordination number is 12, Figure 11). Nevertheless, number of Eu atoms around Sr does not change much and does not exceed 0.5 for as-synthetized samples and 1 for annealed samples. As-synthetized sample with highest Eu

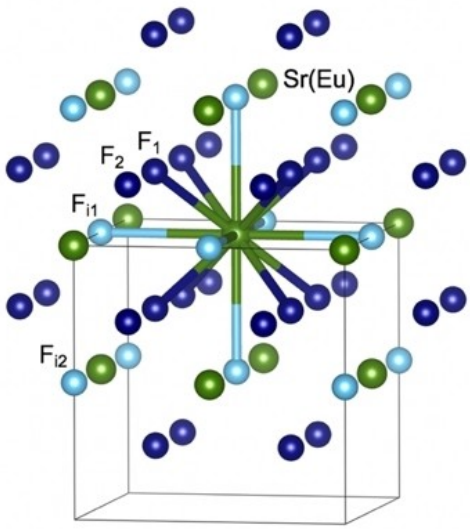

Figure 10. Sr and Eu coordination environment in $Sr_{1-x}Eu_xF_{2+x}$ cubic fluorite structure along *b* crystallographic direction. Sr is shown as green (Eu ions occupy the same crystallographic positions); dark blue – normal F fluorides from the first (F_1, connected with bonds to show the shortest contacts) and second (F_2, do not connected with bonds) coordination spheres; light blue – interstitial F_i fluorides from the first (F_{i1}) and second (F_{i2}) coordination spheres.

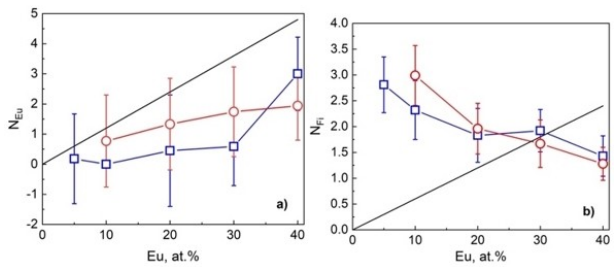

Figure 11. Sr coordination number for Sr…Eu pairs (a) and Sr…F_i^I pairs (b) according to Sr–K EXAFS spectra. Bold lines show regular distribution; ☐ correspond to as synthetized samples; o correspond to heat-treated samples.

content ($Sr_{0.6}Eu_{0.4}F_{2.4}$) show significantly higher Sr–Eu coordination. For annealed samples, N_{Eu} numbers are larger compared to as synthetized samples.

These findings can be explained by decomposition of preformed Eu-containing clusters formed at room temperature in as synthetized samples. Due to clustering, Eu atoms group with surrounding Eu and result in Eu-poor Sr surroundings. With annealing, Eu clusters distributed more in the SrF_2 fluorite matrix.

The number of surrounding interstitial F_i atoms around one Sr atom should theoretically increase linearly from $N_{Fi}=0$ for pristine SrF_2 to $N_{Fi}=0.4\times6=4.8$ for $Sr_{0.6}Eu_{0.4}F_{2.4}$ (maximum coordination number is 6, Figure 11). Nevertheless, N_{Fi} numbers decrease with increasing Eu composition. It can be explained by specific grouping of interstitial F around Eu centers but not around Sr.

Structural data obtained from Eu–L_3 EXAFS spectra contain information only about F_1 and F_i environment of Eu centers. Eu–F distances are systematically smaller in comparison with Sr–F distances, which has been confirmed by decreasing of cell parameters with increased Eu content as well as directly by fitting EXAFS spectra characteristic for Sr and Eu environment (Tables S1 and S2).

Conclusion

The sol-gel synthesis of $Sr_{1-x}Eu_xF_{2-x}$ nanoparticles was initiated from Sr(II) lactate and Eu(III) acetate by reaction with anhydrous HF in in ethylene glycol at room temperature. Heat treatment at 160 °C results in increase of the crystallinity of the particles and an increase of the particle diameter by approximately 50%. Nevertheless, heat treated sols are still transparent and do not show visible precipitation. Interstitial fluoride ions appear in the structure as structural defects and their location is preferably around Eu^{3+} cations. As a result, higher Eu^{3+} concentration results in nanoparticles with higher structural defects and inhomogeneity. Therefore, non-radiative relaxation from other mechanisms is decreased. Eu surrounding does not change much with increasing Eu content. Each Eu^{3+} position has 1–1.7 interstitial F atom (F_i). Heating does not change Eu's occupancy in the crystal structure. Only slight movement to random distribution can be detected. Interstitial F_i anions group around Eu atoms.

For the as-synthesized samples, there is an increase of the luminescence intensity with increasing Eu content up to 40% Eu. For the annealed samples, the luminescence intensity for the particles with the highest Eu content (30% and 40%) decreases drastically. Structural data correlates well these observations. A linear correlation between emission intensity and mean luminescence lifetime shows that the drastic decrease of the emission intensity for the annealed 30 and 40 at.% Eu samples is caused by very effective non-radiative cross-relaxation of the excited states. Such behavior is only possible, when three Eu^{3+} cations can be found in close spatial proximity. Our data show that such probability is higher with Eu atoms forming close clusters with neighboring Eu^{3+} atoms and interstitial F^- anions especially after annealing.

Experimental Section

Chemicals: Europium oxide (Eu_2O_3, 99.9%, Sigma Aldrich), strontium lactate ($Sr(OLac)_2\cdot0.8H_2O$, 98%, Dr. Paul Lohmann; the remaining water was analysed by thermogravimetry), ethylene glycol (99% Sigma Aldrich) and dehydrated methanol (99.8% Sigma Aldrich) were used. Europium acetate was obtained by refluxing the europium oxide with 12 equivalents of 50 vol.% aqueous acetic acid. The product was dried under vacuum for 3 hours at 150 °C to obtain the water-free salt. Pressurised HF gas was obtained from Solvay Fluor. Methanolic HF solution was formed by dissolution of HF gas in water-free methanol provided in a FEP bottle using argon as the carrier gas. The bottle was furnished with a Teflon screw cap with three openings for handling under argon. Tubes were made of stainless steel and PTFE. The HF gas bottle was heated up to 60 °C to ensure a steady flow of HF. The FEP bottle containing the methanol was cooled with ice. The final HF solution in methanol was stored under argon and the concentration was determined by titration with NaOH using phenolphthalein as the indicator. **Caution**! HF is a hazardous agent and has to be used under restricted conditions only.

Synthesis of $Sr_{1-x}Eu_xF_{2-x}$ sols: Doped $Sr_{1-x}Eu_xF_{2-x}$ nanoparticles were prepared in ethylene glycol with $x=0$, 0.01, 0.02, 0.05, 0.1, 0.2, 0.3, 0.4 following the published protocol.[24] Briefly, for preparation of 50 mL of 0.3 M sol of $Sr_{0.9}Eu_{0.1}F_{2.1}$ in ethylene glycol, $Eu(OAc)_3$ (494 mg, 1.50 mmol) and $Sr(OLac)_2\cdot1.01H_2O$ (3833 mg, 13.50 mmol) were dissolved in 46 ml ethylene glycol (OAc = acetate, OLac = lactate). Then, 1.36 mL (31.50 mmol) of a methanolic HF solution (23.3 mol/L) was added under vigorous stirring. After stirring overnight, a transparent colorless sol was received. For convenience, abbreviations for the samples will be used. $Sr_{0.99}Eu_{0.01}F_{2.01}$ = SrF_2:Eu1, $Sr_{0.9}Eu_{0.1}F_{2.1}$ = SrF_2:Eu10 *etc.* The detailed synthesis procedure is described elsewhere.

Heat treatment: All colloidal solutions were heat treated in closed Teflon vessels. For each experiment, 6 ml of colloidal solution was placed in a 10 ml Teflon vessel and closed in steel autoclave. The whole assembly was heated from room temperature to 160 °C with 10 K/min, annealed for 4 hours and naturally cooled to room temperature for 6 hours. In all cases, transparent colourless solutions were obtained and used without any further filtration or purification.

Luminescence spectra: Luminescence emission and excitation spectra as well as lifetimes were recorded with a FluoroMax-4P from Horiba Jobin Yvon in 10 mm quartz cells. Luminescence

lifetimes were recorded in a single photon counting mode using the TCSPC accessory with a collecting time up to 175 ms (λ_{ex} = 393 nm, λ_{ex} = 590 nm). Fitting the luminescence lifetimes with a single monoexponential decay was not possible. This is typical for nanoparticles, because luminescence centres in the middle or near the surface of the particle have significantly different decay behaviours. Instead, lifetimes were fitted using a biexponential function

$$I(t) = A_1 e^{-\frac{t}{\tau_1}} + A_2 e^{-\frac{t}{\tau_2}} + C$$

with mean lifetime as

$$\tilde{\tau} = \frac{A_1\tau_2 + A_2\tau_2}{A_1 + A_2}.$$

X-ray absorption spectroscopy (XAS): X-ray absorption near edge structure (XANES) and extended X-ray fine structure (EXAFS) spectroscopy at the Sr–K absorption edge (16.105 keV) for all colloidal solutions were collected at BL8 beamline located at the DELTA synchrotron facility at the TU Dortmund (Dortmund, Germany).[26] Liquid samples were placed in a transmission cell with 0.05 mm Kapton windows with a fixed distance between windows of 3 mm. As-synthesized and heat-treated samples were measured at room temperature. Powder of $SrCl_2 \cdot 6H_2O$ (Sigma Aldrich) mixed with hexagonal BN was used as external standard for energy calibration.

XANES and EXAFS spectra on Eu-L_3 absorption edge (6.977 keV) have been collected at the BL10 located at the DELTA synchrotron facility at the TU Dortmund (Dortmund, Germany).[27] Liquid samples were measured in similar transmission cells with distance between windows fixed at 1 mm. Powder of Eu_2O_3 mixed with hexagonal BN was used as external standard for energy calibration.

Typically, for each sample and each absorption edge, 3 measurements were performed and further averaged to improve statistics. Data evaluation, analysis and simulation have been performed using the IFEFFIT software.[28,29]

X-ray diffraction: As-synthesized and heat-treated samples were characterised using X-ray diffraction. Liquid sols were sealed in 1 mm borosilicate glass capillaries (Müller GmbH, Berlin, Germany) and measured with spinning at room temperature (λ = 0.20714 Å); LaB_6 powder was used as external standard for wavelength and sample-to-detector distances calibration. Measurements were performed at the P02.1 beamline at the PETRA III synchrotron facility (DESY, Hamburg, Germany).[30] Capillaries filled with pure ethylene glycol were used for background subtraction. Data reduction and integration has been performed using DAWN.[31,32] Background was subtracted using GUDRUN.[33] For each sample, 15 diffractograms were collected and averaged to obtain better signal to noise ratio. Rietveld refinements were performed using TOPAS.[34] Profile parameters for the Lorentzian function, cell parameters, atomic occupancies and isotropic atomic displacements were refined simultaneously.

Small-angle X-ray scattering: The scattering curves for as-synthetized and heat-treated samples were measured in house on a Kratky-type SAXS instrument (SAXSess, Anton Paar, Graz, Austria) equipped with a sealed Cu X-ray tube ($\lambda_{CuK\alpha}$ = 1.542 Å) and a microstrip X-ray detector (Mythen2 R detector system, Dectris, Baden-Dättwil, Switzerland). The measured intensity was corrected for background contributions and slit smearing effect using the software package SAXSquant4.2. (Anton Paar). Liquid samples were placed in 1 mm quartz capillaries; an empty capillary and a capillary filled with pure solvent (ethylene glycol) were used for background correction. The SAXS data analysis was performed with the SASfit program package 0.94.11[35] using a model function that describes a homogeneous sphere with a Schulz-Zimm size distribution.

Transmission electron microscopy: Transmission electron microscopy (TEM) images were obtained in a Talos F200S Microscope (Thermo Fisher Scientific) by using a 200 kV microscopy technique in which a beam of electrons is transmitted through a specimen to form an image. Samples were diluted with methanol and droped onto a 3 mm copper grid (lacey, 400 mesh) and leaving them to air-dry at room temperature.

Acknowledgements

The authors acknowledge the BAM funding program "Ideas" (Menschen Ideen): New insights on the thermal behavior of luminescent nanoparticles from Sol-Gel synthesis by in situ characterization – towards efficient upconversion. X-ray diffraction studies have been carried out at the P02.1 beamline of the PETRA III synchrotron facility at DESY (Hamburg), a member of the Helmholtz Association (HGF). X-ray absorption spectroscopy studies were performed at the BL8 and BL10 beamlines at the DELTA synchrotron facility (Technische Universität Dortmund, Dortmund, Germany). Open Access funding enabled and organized by Projekt DEAL.

Conflict of Interest

The authors declare no conflict of interest.

Keywords: strontium fluoride · europium fluoride · nanoparticles · luminescence · EXAFS

[1] H. Bill, G. Calas, *Phys. Chem. Miner.* **1978**, *3*, 117–131.
[2] B. P. Sobolev, *Crystallogr. Rep.* **2012**, *57*, 434–454.
[3] B. P. Sobolev, K. B. Seiranian, *J. Solid State Chem.* **1981**, *39*, 337–344.
[4] B. P. Sobolev, K. B. Seiranian, L. S. Garashina, P. P. Fedorov, *J. Solid State Chem.* **1979**, *28*, 51–58.
[5] M. Y. Gryaznov, S. V. Shotin, V. N. Chuvil'deev, M. O. Marychev, E. A. Sul'yanova, S. N. Sul'yanov, B. P. Sobolev, *Crystallogr. Rep.* **2012**, *57*, 144–150.
[6] B. P. Sobolev, N. I. Sorokin, *Crystallogr. Rep.* **2014**, *59*, 807–830.
[7] B. P. Sobolev, N. I. Sorokin, N. B. Bolotina, in *Photonic and Electronic Properties of Fluoride Materials* (Eds.: A. Tressaud, K. Poeppelmeier), Elsevier, Boston, 2016, DOI: https://doi.org/10.1016/B978-0-12-801639-8.00021-0, pp. 465–491.
[8] S. Gai, C. Li, P. Yang, J. Lin, *Chem. Rev.* **2014**, *114*, 2343–2389.
[9] J. Zhou, Q. Liu, W. Feng, Y. Sun, F. Li, *Chem. Rev.* **2015**, *115*, 395–465.
[10] P. P. Fedorov, S. V. Kuznetsov, V. V. Osiko, in *Photonic and Electronic Properties of Fluoride Materials*, (Eds.: A. Tressaud, K. Poeppelmeier), Elsevier, Boston, 2016, DOI: https://doi.org/10.1016/B978-0-12-801639-8.00002-7, pp. 7–31.
[11] B. Ritter, P. Haida, F. Fink, T. Krahl, K. Gawlitza, K. Rurack, G. Scholz, E. Kemnitz, *Dalton Trans.* **2017**, *46*, 2925–2936.
[12] P. Cortelletti, M. Pedroni, F. Boschi, S. Pin, P. Ghigna, P. Canton, F. Vetrone, A. Speghini, *Cryst. Growth Des.* **2018**, *18*, 686–694.
[13] A. K. Cheetham, B. E. F. Fender, M. J. Cooper, *J. Phys. C* **1971**, *4*, 3107–3121.
[14] J. P. Laval, A. Mikou, B. Frit, G. Roult, *Solid State Ionics* **1988**, *28–30*, Part 2, 1300–1304.

[15] M. Ito, C. Goutaudier, Y. Guyot, K. Lebbou, T. Fukuda, G. Boulon, *J. Phys. Condens. Matter* **2004**, *16*, 1501–1521.
[16] L. P. Otroshchenko, V. V. Aleksandrov, N. N. Bydanov, V. I. Simonov, B. P. Sobolev, *Kristallografiya* **1988**, *33*, 764–765.
[17] N. B. Grigor'eva, L. P. Otroshchenko, B. A. Maskimov, I. A. Verin, B. P. Sobolev, V. I. Simonov, *Crystallogr. Rep.* **1996**, *41*, 697–713.
[18] B. Ritter, T. Krahl, G. Scholz, E. Kemnitz, *J. Phys. Chem. C* **2016**, *120*, 8992–8999.
[19] A. Antuzevics, M. Kemere, G. Krieke, *J. Alloys Compd.* **2018**, *762*, 500–507.
[20] T. Krahl, G. Scholz, E. Kemnitz, *J. Phys. Chem. C* **2014**, *118*, 21066–21074.
[21] F. Wang, X. Fan, D. Pi, M. Wang, *Solid State Commun.* **2005**, *133*, 775–779.
[22] J. Wang, W. Miao, Y. Li, H. Yao, Z. Li, *Mater. Lett.* **2009**, *63*, 1794–1796.
[23] P. Samuel, H. Ishizawa, Y. Ezura, K. I. Ueda, S. M. Babu, *Opt. Mater.* **2011**, *33*, 735–737.
[24] T. Krahl, F. Beer, A. Relling, K. Gawlitza, K. Rurack, E. Kemnitz, *ChemNanoMat* **2020**, *6*, 1086–1095.
[25] C. R. Ronda, in *Luminescence*, Wiley VCH, Weinheim, 2007, DOI: 10.1002/9783527621064.ch1, pp. 1–34.
[26] D. Lützenkirchen-Hecht, R. Wagner, U. Haake, A. Watenphul, R. Frahm, *J. Synchrotron Radiat.* **2009**, *16*, 264–272.
[27] D. Lützenkirchen-Hecht, R. Wagner, S. Szillat, A. K. Hüsecken, K. Istomin, U. Pietsch, R. Frahm, *J. Synchrotron Radiat.* **2014**, *21*, 819–826.
[28] B. Ravel, M. Newville, *J. Synchrotron Radiat.* **2005**, *12*, 537–541.
[29] M. Newville, *J. Synchrotron Radiat.* **2001**, *8(2)*, 322–324.
[30] A.-C. Dippel, H.-P. Liermann, J. T. Delitz, P. Walter, H. Schulte-Schrepping, O. Seeck, H. Franz, *J. Synchrotron Radiat.* **2015**, *3*, 675–687.
[31] M. Basham, J. Filik, M. T. Wharmby, P. C. Y. Chang, B. El Kassaby, M. Gerring, J. Aishima, K. Levik, B. C. A. Pulford, I. Sikharulidze, D. Sneddon, M. Webber, S. S. Dhesi, F. Maccherozzim, O. Svensson, S. Brockhauser, G. Naray, A. W. Ashton, *J. Synchrotron Radiat.* **2015**, *22*, 853–858.
[32] J. Filik, A. W. Ashton, P. C. Y. Chang, P. A. Chater, S. J. Day, M. Drakopoloulos, M. V. Gerring, M. L. Hart, O. V. Magdysyuk, S. Michalik, A. Smith, C. C. Tang, N. J. Terrill, M. T. Wharmby, H. Wilhelm, *J. Appl. Crystallogr.* **2017**, *50*, 959–966.
[33] A. K. Soper, E. R. Barney, *J. Appl. Crystallogr.* **2011**, *44*, 714–726.
[34] TOPAS v.4.0, Bruker-AXS 5465 East Cheryl Parkway – Bruker AXS, 2009.
[35] I. Bressler, J. Kohlbrecherand, A. F. Thünemann, *J. Appl. Crystallogr.* **2015**, *48*, 1587–1598.

Manuscript received: July 8, 2021
Accepted manuscript online: August 6, 2021
Version of record online: September 12, 2021